AGU PUBLICATIONS

JGR

Journal of Geophysical Research: Atmospheres

RESEARCH ARTICLE
10.1002/2014JD022585

Key Points:
- Spatiotemporal features of Holocene East Asian winter monsoon
- High-latitude forcing of the EAWM in northwestern China
- Low-latitude forcing of the EAWM on eastern Tibetan Plateau and in southern China

Correspondence to:
L. Jin,
jinly@lzu.edu.cn

Citation:
Zhang, X., L. Jin, and N. Li (2015), Asynchronous variation in the East Asian winter monsoon during the Holocene, *J. Geophys. Res. Atmos.*, *120*, 5357–5370, doi:10.1002/2014JD022585.

Received 15 SEP 2014
Accepted 30 APR 2015
Accepted article online 5 MAY 2015
Published online 2 JUN 2015

Asynchronous variation in the East Asian winter monsoon during the Holocene

Xiaojian Zhang[1], Liya Jin[1], and Na Li[1]

[1]Key Laboratory of Western China's Environmental Systems, Lanzhou University, Lanzhou, China

Abstract The East Asian winter monsoon (EAWM) is one of the most active components of the global climate system. Climate anomalies associated with the EAWM differ between extratropical and tropical regions due to the EAWM's meridional extent. Spatial differences in the EAWM variability on centennial and millennial time scales during the Holocene have not been well understood. This study describes Holocene spatiotemporal features of the EAWM based on comparisons of proxy records and climate simulations. The analysis specifically compared four proxy records located throughout China to assess the EAWM's spatial variability during the Holocene. These records indicate a stronger EAWM during the early Holocene than that during the late Holocene. The EAWM also shows a rapid, asynchronous decline from northwestern to southeastern China. The EAWM declined in northwestern China from 10 to 7.5 ka B.P., whereas the decline did not occur in southern China and the eastern Tibetan Plateau until 6–4.5 ka B.P. Coupled equilibrium and transient simulations of climate evolution during the Holocene indicate that the decline of the EAWM from 10 to 7.5 ka B.P. was probably caused by melting of Northern Hemisphere (NH) ice sheets and enhanced Atlantic meridional overturning circulation (AMOC). The decline of the EAWM from 6 to 4.5 ka B.P. over the eastern Tibetan Plateau and southern China is related to an abrupt increase in sea surface temperatures (SSTs) of the tropical western Indian Ocean. We therefore argue that the regional shift in EAWM intensity was probably related to a distinguishing response to high-latitude (NH ice sheets and AMOC) and low-latitude (tropical SSTs) forcings.

1. Introduction

The Asian monsoon is one of the most powerful phenomena presently operating in Earth's climate system and plays a significant role in global climate variability on a range of different time scales [*Wang*, 2006]. During the boreal winter, the powerful Siberian-Mongolian high (SH) stationed over Eurasia generates strong northwesterly winds that course over East Asia. These are referred to as the East Asian winter monsoon (EAWM). The intensity of this system influences temperature and precipitation variation throughout eastern China, Korea, Japan, and surrounding areas, and thus exerts profound economic and social impacts on the region [*J. Sun et al.*, 2010; *Wang et al.*, 2011]. At the surface, the EAWM specifically consists of the cold-core SH, the Aleutian Low, the large meridional gradient of surface temperatures observed over East Asia, and prevailing low-level northwesterly winds associated with the SH's anticyclonic circulation along East Asian coastal areas (Figure 1).

Numerous studies have addressed EAWM variability on interannual and interdecadal time scales. These have conducted various types of analysis on modern meteorological observations that span periods dating as far back as 60 years. Consensus holds that the current EAWM is primarily driven by continent-scale differences in heat absorption by the Eurasian continent and adjacent oceans [*Webster*, 1987; *Young*, 1987]. A strong EAWM is characterized by a strong SH [e.g., *Ding*, 1990; *Zhang et al.*, 1997; *Wu et al.*, 2006], which closely relates to the negative phase of the Arctic Oscillation [e.g., *Wu and Huang*, 1999; *Gong et al.*, 2001; *Wu and Wang*, 2002; *Chen et al.*, 2013]. Eurasian snow cover is a precursory signal for the winter monsoon [e.g., *Watanabe and Nitta*, 1999; *Clark and Serreze*, 2000; *Gong et al.*, 2003; *Jhun and Lee*, 2004; *Wang et al.*, 2010]. High levels of autumn snow cover increase albedo, reduce the surface solar radiation flux, and lower air temperatures to create an enhanced SH during autumn and the ensuing winter. These factors thus induce a strong EAWM [*Wang et al.*, 2010]. Changes in sea surface temperatures (SSTs) associated with El Niño–Southern Oscillation (ENSO) events are also considered to be an important driving factor contributing to EAWM variability. The EAWM tends to be weaker during El Niño and stronger during La Niña years [e.g., *Tomita and Yasunari*, 1996; *Zhang et al.*, 1996; *Chen et al.*, 2000; *Wang et al.*, 2000; *He et al.*, 2008; *Chen et al.*, 2013, 2014].

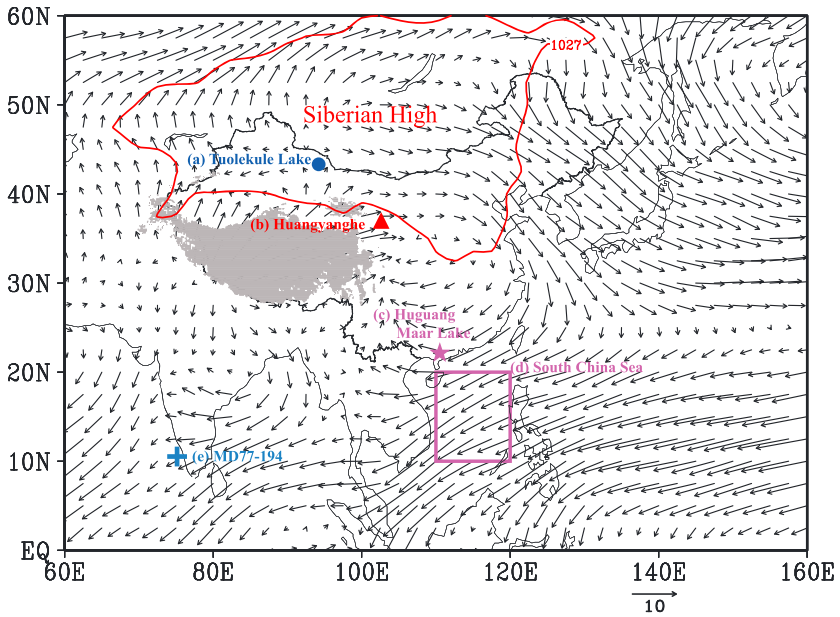

Figure 1. Areas covered by proxy records for Holocene EAWM and SSTs interpreted in this study. Near surface air circulation patterns are shown as 925 hPa wind field vectors (m/s; arrows). The red curved line is the extent of the 1027 hPa isobar (SLP) during the boreal winter (December-January-February) from 1949 to 2008 based on National Centers for Environmental Prediction/National Center for Atmospheric Research (NCEP/NCAR) reanalysis [*Kalnay et al.*, 1996]. Proxy records are as follows: (a) Tuolekule Lake (43.3°N, 94.2°E) [*An et al.*, 2011], (b) Huangyanghe (37.42°N, 102.6°E) [*Li and Morrill*, 2014], (c) Huang Maar Lake (21.15°N, 110.3°E) [*Wang et al.*, 2012], (d) South China Sea (10–20°N, 110–120°E) [*Huang et al.*, 2011], and (e) core MD77-194 (10.4667°N, 75.2333°E) [*Sonzogni et al.*, 1998].

Long-term variation in the Asian monsoon has attracted considerable attention due to its implications for global climate. The grain size sequences of Chinese loess deposits are a classic proxy for reconstructing long-term changes in EAWM intensity [e.g., *Porter and An*, 1995; *Liu and Ding*, 1998; *An*, 2000; *Sun et al.*, 2010a, 2010b; *Shi et al.*, 2011]. EAWM signals have also been interpreted from marine sediment cores e.g., northern South China Sea (SCS) [*Wang et al.*, 1999; *Steinke et al.*, 2011], the Sulu Sea [*de Garidel-Thoron et al.*, 2001], the southern SCS [*Tian et al.*, 2005; *Steinke et al.*, 2010; *Huang et al.*, 2011], lake sediments [*Yancheva et al.*, 2007; *Wang et al.*, 2008, 2012], and peat sequences [*Yu et al.*, 2011]. Geochemical and biostratigraphic proxies from Chinese loess deposits and lake sediments have given conflicting information concerning EAWM intensity. Titanium concentrations and diatom assemblages from Huguang Maar Lake, for example, gave opposing information concerning EAWM strength during the Holocene [*Yancheva et al.*, 2007; *Wang et al.*, 2012]. Titanium contents of Huguang Maar Lake sediments may derive from runoff however, and thus reflect local signatures of the catchment rather than the regional influence of the EAWM [*Zhou et al.*, 2007, 2009; *Han et al.*, 2010]. On the whole, the proxies described here integrate into a regional record that gives a consistent picture of EAWM variation.

It is generally believed that EAWM variation is closely linked to changes in Northern Hemisphere (NH) ice volume at orbital time scales [*Ding et al.*, 1994, 1995; *Liu and Ding*, 1998; *Porter*, 2001], which itself is linked to summer insolation at 65°N [*Hays et al.*, 1976; *Imbrie et al.*, 1984; *Ruddiman et al.*, 1989; *Shackleton et al.*, 1990]. Around the beginning of the Holocene epoch (12 to 11.5 ka B.P.), NH ice sheets were retreating rapidly [*Peltier*, 2004; *Lisiecki and Raymo*, 2005] in spite of a decrease in summer insolation [*Berger and Loutre*, 1991] with the remnant Laurentide ice sheets (LIS) disappearing by 7 ka B.P. [*Peltier*, 2004]. The impact of the NH glacial retreat on East Asia (e.g., on the EAWM) was negligible during the middle and late Holocene. Changes in the EAWM are also attributed to Atlantic meridional overturning circulation (AMOC) via northern westerlies [*Sun et al.*, 2012].

Modern climatological studies of annual to multidecadal records have interpreted the EAWM system as a coupled extratropical-tropical system, extending from the SH all the way down to the equatorial SCS [*Wang et al.*, 2010]. Extratropical and tropical East Asian climate anomalies related to the EAWM exhibit

Table 1. Summary of Holocene Winter Monsoon Proxy Records Interpreted in the Study

ID	Name	Latitude (°N)	Longitude (°E)	Proxy Type	Dating Method	Number of Holocene Age Constraints in Record	Modern Process Study	Reference
1	Tuolekule Lake	43.3	94.2	Grain size	AMS ^{14}C[a]	6	Yes	*An et al.* [2011]
2	Huangyanghe	37.42	102.6	Total organic carbon	AMS ^{14}C	9	No	*Li and Morrill* [2014]
3	Huguang Maar Lake	21.15	110.3	Diatom	AMS ^{14}C	5	Yes	*Wang et al.* [2012]
4	South China Sea	10–20	110–120	SST gradient	AMS ^{14}C	9	Yes	*Huang et al.* [2011]

[a]AMS ^{14}C, Accelerator mass spectrometry ^{14}C ages.

some variation due to the large meridional extent of the EAWM [*Wang et al.*, 2010; *Chen et al.*, 2014]. These differences are specifically characterized as northern and southern modes of the anomaly [*Wang et al.*, 2010; *Chen et al.*, 2014] and apparently arise from different driving mechanisms. The northern mode is closely related to snow cover in southern Siberia-Mongolia, whereas the southern mode relates to the ENSO [*Wang et al.*, 2010]. Beyond those listed above, few studies have investigated driving mechanisms for spatial differences in EAWM variability during the Holocene. To address this gap, this study interprets four Holocene proxy records for the EAWM, as it occurs in northwestern China, the eastern Tibetan Plateau, and southern China. Proxy data are compared to results from coupled equilibrium and transient simulations of Holocene climate. Together, these are used to explore potential driving mechanisms for the spatial variability of rapid changes in the EAWM during the Holocene.

2. Methods

2.1. Proxy Records

Four recently published, high-resolution and chronologically well-constrained proxy records (Table 1 and Figure 1) spanning most of the Holocene (10–0 ka B.P.) were analyzed for signs of EAWM variation. Mean grain size of aeolian sediment from lacustrine (Tuolekule Lake) and arid, continental environments in northern China records the strength of the SH and, by extension, EAWM intensity [*An et al.*, 2011]. EAWM influence may extend to the equator [*Wang et al.*, 2010] via northerly winds coursing over eastern China (Figure 1). The strength of the northerly winds is, therefore, interpreted as an indicator of EAWM intensity [*Ji et al.*, 1997; *Chen and Sun*, 1999; *Lu and Chan*, 1999; *Chen et al.*, 2000; *Hu et al.*, 2000; *Yang et al.*, 2002] and one recorded by Holocene sediments (Huguang Maar Lake and SCS localities). Strong northerly winds disturb surface waters, increase dissolved oxygen, and stimulate growth of diatom populations. Sedimentary diatom assemblages in Huguang Maar Lake record the strength of the EAWM [*Wang et al.*, 2012]. Strong northerly winds also transport cold water from the northern SCS, amassing it off the coast of southern Vietnam. Mixing and diffusing then transfers the cold water to the southeastern SCS [*Liu et al.*, 2004; *Huang et al.*, 2011]. Interpreting a variety of alkenone-based sea surface temperature (SST) indicators, *Huang et al.* [2011] found significant evidence of these "cold tongues" off southern Vietnam, in the east-west SST gradient of the southern SCS. Cold tongue development is strongly influenced by wind-driven southward advection of cold surface water. The spread of the cold upper ocean waters expands the cold tongue area, enhances the east-west SST gradient, and offers a clear indication of variations in EAWM intensity [*Huang et al.*, 2011]. Both the diatom record from Huguang Maar Lake [*Wang et al.*, 2012] and the east-west SST gradient in the SCS [*Huang et al.*, 2011] are significantly correlated with the modern EAWM index. *Li and Morrill* [2014] used grain size distributions, total organic carbon (TOC), magnetic susceptibility, and carbonate content of two aeolian sedimentary profiles in Huangyeanghe to

Table 2. Summary of Holocene SST Proxy Records Interpreted in the Study

ID	Name	Latitude(°N)	Longitude (°E)	Proxy Type	Dating Method	Reference
1	MD77-194	10.4667	75.2333	Alkenone	Isotope stratigraphy	*Sonzogni et al.* [1998]
2	BOFS31K	19	−20.167	Alkenone	Isotope stratigraphy	*Zhao et al.* [1995]
3	GeoB7926-2	20.217	−18.45	Alkenone	AMS ^{14}C	*Romero et al.* [2008]
4	OCE326-GGC26	43.483	−54.867	Mg/Ca	AMS ^{14}C	*Sachs* [2007]
5	MD99-2251	57.433	−27.9	Mg/Ca	AMS ^{14}C	*Farmer et al.* [2011]
6	ODP162-984	61	−25	Mg/Ca	AMS ^{14}C	*Came et al.* [2007]

Table 3. CCSM3 8.5 ka Simulation Conditions

	Eccentricity	Obliquity	Precession	CO_2 (ppm)	CH_4 (ppb)	N_2O (ppb)	LIS	St. Lawrence Meltwater Flux
Exp_8.5 ka	0.019199	24.22°	319.50°	260	660	260	None	None
Exp_8.5 $ka_{MELTICE}$	Same as Exp_8.5 ka						*Peltier* [2004]	0.05 Sv[a]

[a]Sv, sverdrup (10^6 m^3/s).

reconstruct Holocene EAWM history for the eastern Tibetan Plateau. We used the data from Profile b in our analysis due to its excellent chronostratigraphic constraint [*Li and Morrill*, 2014]. The EAWM patterns revealed by these proxies behave in a similar manner, allowing us to confine our analysis to the TOC proxy. Total organic carbon is an accurate proxy because a strong winter monsoon reduces plant growth in the subsequent year and is not conducive to preservation of organic matter [*Xiao et al*., 2002].

To explore the possible driving mechanisms for variations in the EAWM, we included a global ice sheet reconstruction (ICE-5G) [*Peltier*, 2004], as well as a core (OCE326-GGC5) from the Bermuda Rise that serves as a proxy for AMOC strength in the deep western subtropical Atlantic [*McManus et al*., 2004]. We also used six SST proxy records (Table 2). *Leduc et al*. [2010] suggested that Mg/Ca records from North Atlantic sediments north of 30°N record winter SSTs, as do alkenone records from cores collected between 20°S and 30°N. We therefore used Mg/Ca data from cores OCE326-GGC26 (43.483°N, 54.867°W), MD99-2251 (57.433°N, 27.9°W), and ODP162-984 (61°N, 25°W), and alkenone data from cores MD77-194 (10.4667°N, 75.2333°E), BOFS31K (19°N, 20.167°W), and GeoB7926-2 (20.217°N, 18.45°W).

2.2. Modeling Data

We compared proxy data to two model simulations of Holocene climate change from *Jin et al*. [2012, 2014]. One data set derives from a coupled ocean-atmosphere-sea ice-land surface climate model (v. 3) of the Community Climate System Model (CCSM3, T31 resolution) [*Yeager et al*., 2006], with a component of LIS and St. Lawrence meltwater flux at 8.5 ka B.P. (Table 3) [*Jin et al*., 2012]. This model was used to investigate the effects of NH ice volume and AMOC on the EAWM. The other [*Jin et al*., 2014] is a transient simulation (HT) based on orbital forcing parameters (Table 4) for the period of 9.5–0 ka B.P. with a tenfold acceleration scheme [*Lorenz and Lohmann*, 2004] simulated by the Kiel Climate Model (KCM) [*Park et al*., 2009]. This simulation assumed a coupled atmosphere-ocean general circulation model consisting of the European Centre/Hamburg (ECHAM5) spectral atmospheric model and the Nucleus for European Modeling of the Ocean (NEMO) ocean-sea-ice general circulation model, coupled using OASIS3. The horizontal resolution of ECHAM5 is T31 (3.75° × 3.75°) with 19 levels of vertical resolution up to 10 hPa. The horizontal resolution of NEMO is 1.3° on average, based on 2° Mercator meshes with grid refinement in the tropics, where the meridional grid point separation reaches 0.5°. In addition, the Twentieth Century Reanalysis (20thCR, v. 2) [*Compo et al*., 2011] and Centennial Observation-Based Estimates of SST (COBE-SST2, v. 2) data products [*Hirahara et al*., 2014] were used to identify possible physical mechanisms for the observed EAWM variability. The 20thCR uses monthly SSTs and subdaily sea surface pressure (SLP) observations to reconstruct global climate at subdaily temporal resolution and on a 2.0° × 2.0° grid over a period spanning from 1871 to 2012. *Zhang et al*. [2013] have carefully examined 20thCR performance in reproducing spatial patterns and temporal variability of the EAWM. They found that 20thCR data can accurately reproduce typical configuration patterns of all subfactors involved in the EAWM system. It also accurately reproduces the relatively short time scales (<10 year) on which EAWM variability operates. The COBE-SST2 includes monthly SST data on a 1.0° × 1.0° grid for a period spanning from 1850 to 2013 and adjusts for SST bias using annually and globally averaged data.

Table 4. KCM Holocene Simulation Conditions

	Eccentricity	Obliquity	Precession	CO_2 (ppm)	CH_4 (ppb)	N_2O (ppb)
H0K	0.0167	23.4°	102°	286.2	805.6	276.7
H9K	0.0194	24.2°	303°		Same as H0K	
HT	Varying from H9K to H0K				Same as H0K	

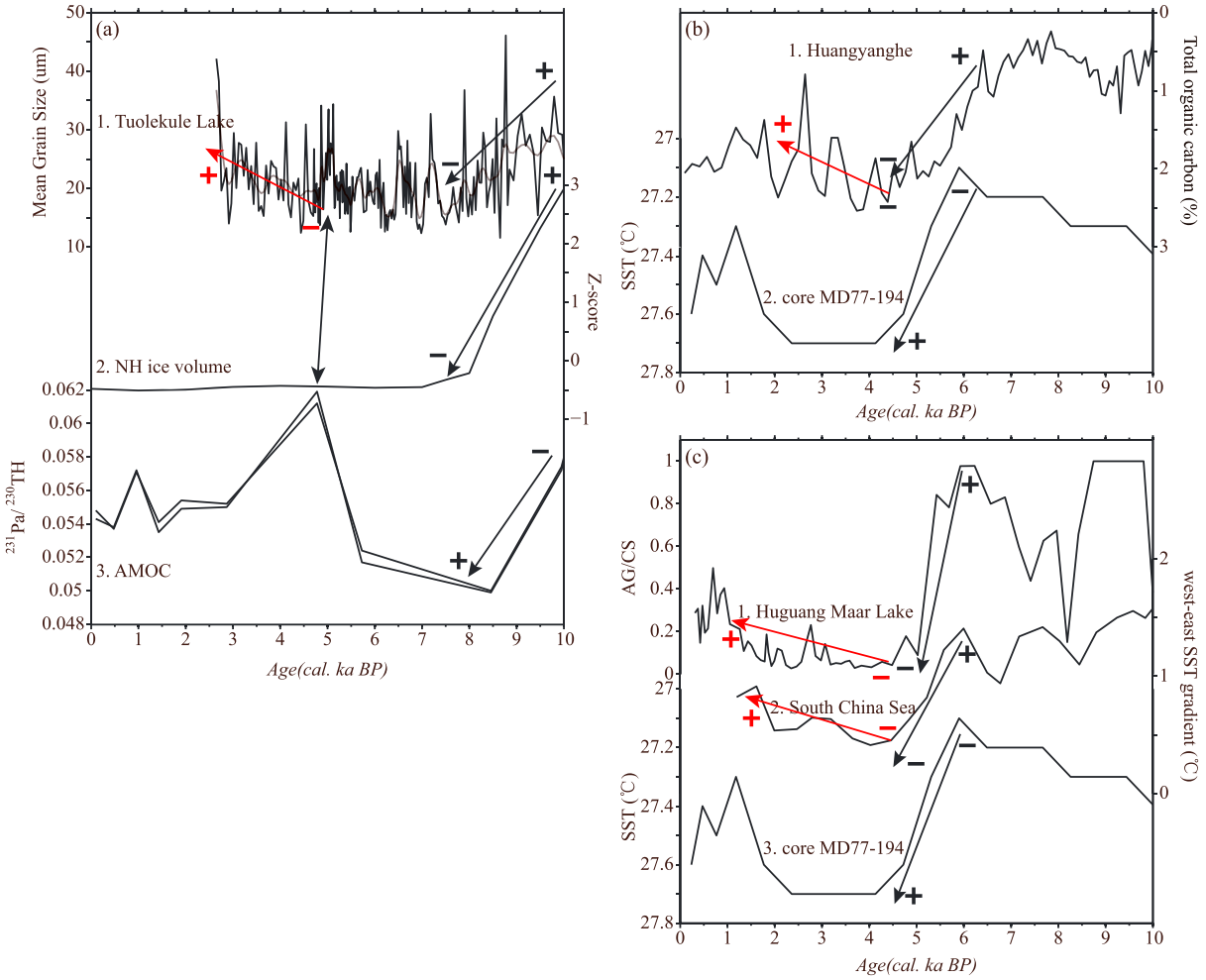

Figure 2. Comparisons of Holocene EAWM proxy records. (a) Mean grain size (μm) from Tuolekule Lake (43.3°N, 94.2°E) sediments [*An et al*., 2011] (a1), Northern Hemisphere (NH) ice volume (*Z* score) [*Peltier*, 2004; *Lisiecki and Raymo*, 2005] (a2), and Atlantic meridional overturning circulation (AMOC) (^{231} Pa/^{230}Th) [*McManus et al*., 2004] (a3). b Proxy data of total organic carbon (TOC; %) from Huangyanghe (37.42°N, 102.6°E) [*Li and Morrill*, 2014] (b1) and sea surface temperature (SSTs; °C) from the western Indian Ocean (WIO) (core MD77-194, 10.4667°N, 75.2333°E) [*Sonzogni et al*., 1998] (b2). (c) Diatom proxy data measured as AG/CS (the ratio between *Aulacoseira granulata* and *Cyclotella stelligera*) from Huang Maar Lake (21.15°N, 110.3°E) [*Wang et al*., 2012] (c1), the east-west SST gradient (°C) between the southwestern and southeastern SST arrays from the South China Sea (10–20°N, 110–120°E) [*Huang et al*., 2011] (c2), and WIO SSTs (°C) from core MD77-194 (10.4667°N, 75.2333°E) [*Sonzogni et al*., 1998] (c3). Red and black arrows indicate changing trends.

3. Proxy Results

Figure 2 shows that proxy records give the spatial pattern for EAWM variability during the Holocene. The mean grain size proxy from Tuolekule Lake shows a rapid decline in EAWM intensity over northwestern China from 10 to 7.5 ka B.P. (Figure 2a1). The TOC proxy from the Huangyanghe core shows a rapid decline in EAWM intensity over the eastern Tibetan Plateau from 6 to 4.5 ka B.P. (Figures 2b1). Diatom assemblages from Huguang Maar Lake (Figure 2c1) and east-west SST gradient from the SCS (Figure 2c2) also show the EAWM decline in intensity at 6–4.5 ka B.P. Together, these trends demonstrate the asynchronous evolution of the EAWM in northern and southern China during the Holocene. From 4.5 to 2 ka B.P., all of the EAWM proxy records show strengthening of the EAWM (Figure 2, red arrows).

Changing NH ice volume [*Ding et al*., 1994, 1995; *Liu and Ding*, 1998; *Porter*, 2001] and AMOC strength [*Sun et al*., 2012] are considered to be key drivers for EAWM variations on orbital time scales. During the early Holocene (10–7.5 ka B.P.), the rapid decline in NH ice volume (Figure 2a2) [*Peltier*, 2004; *Lisiecki and Raymo*, 2005] and stronger AMOC (Figure 2a3) [*McManus et al*., 2004] could have significantly weakened the SH, leading to a decline in EAWM intensity near the center of the SH. These mechanisms are evident from

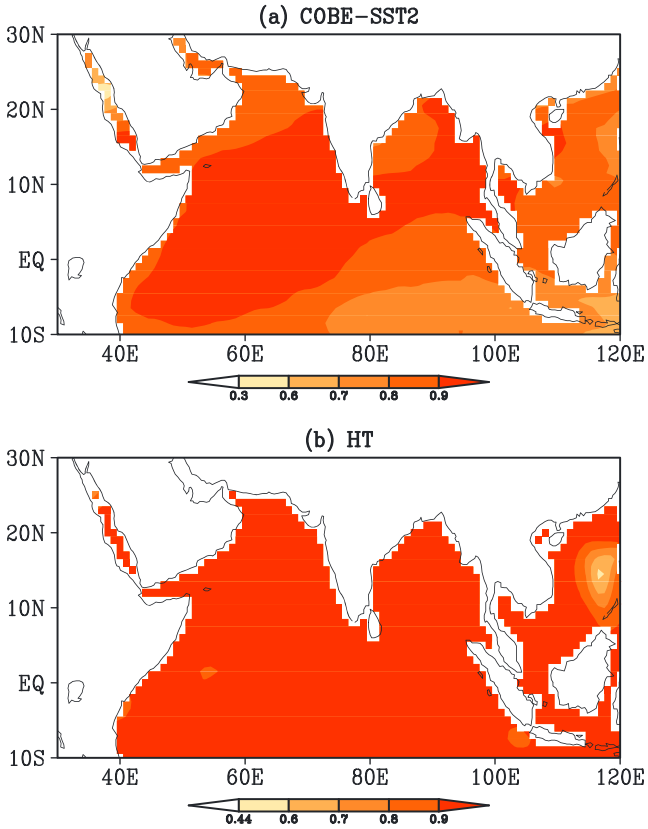

Figure 3. Maps showing correlation between the winter SST at core MD77-194 and Indian Ocean SSTs from 1872 to 2012 on (a) interdecadal time scales and from 9.5–0 ka BP on (b) millennial time scales. The 1872–2012 SST data come from COBE-SST2, and the more extensive Holocene data come from the KCM Holocene transient simulation (see section 2.2). Shaded areas indicate correlation coefficients that are significant at the 5% significance level as estimated using Monte Carlo methods [*Livezey and Chen*, 1983; *Di Lorenzo et al.*, 2010].

the longer-term relationship between NH ice volume [*Ding et al.*, 1995], AMOC [*Sun et al.*, 2012], and EAWM variation. Furthermore, a strong EAWM corresponds to a weak AMOC at about 5 ka B.P. (Figure 2a3).

With the disappearance of the remnant LIS at 7 ka B.P. [*Peltier*, 2004; *Lisiecki and Raymo*, 2005], the influence of NH ice volume on EAWM may have gradually subsided. Records show a rapid decline in EAWM intensity during the mid-Holocene (around 6.0–4.0 ka B.P.) on the eastern Tibetan Plateau (Figure 2b1) and in southern China (Figures 2c1 and 2c2). The rapid increase in western Indian Ocean (WIO) SSTs (derived from core MD77-194, Figures 2b2 and 2c3) mirrors the rapid decline in EAWM intensity at 6.0–4.0 ka B.P. (Figures 2b1, 2c1, and 2c2). Although this study considered only one data proxy for WIO SSTs, SSTs at the location of the record correlate well with both observed modern day and simulated Holocene WIO SSTs (Figures 3a and 3b, respectively), such that the data are assumed to provide reasonable estimates of winter WIO SSTs.

4. Discussion

An et al. [2011] showed that mean grain size of aeolian sediments from Tuolekule Lake (Figures 1 and 2a1) correlated with variation in SH intensity with greater mean grain size reflecting a stronger SH and intensified EAWM. During the early Holocene (10–8.5 ka B.P.), larger mean grain sizes from aeolian sediments (Figure 2a1) coincide with greater NH ice volume (Figure 2a2) and weaker AMOC (Figure 2a3). The coupled climate model CCSM3 equilibrium 8.5 ka simulation, which assumed additional NH ice volume (LIS) and weaker AMOC (St. Lawrence meltwater flux) (Exp_8.5 ka $_{\text{MELTICE}}$ minus Exp_8.5 ka, Table 3) as inputs, showed positive SLP anomalies for the Eurasian continent (Figure 4a) and a resultant strong winter monsoon, further demonstrating the influence of NH ice sheets and AMOC on EAWM intensity.

To explore the potential influence of tropical SSTs on the EAWM, we defined an EAWM index (EAWM_S index) with boreal winter (December-January-February, DJF) northerly mean winds averaged over the region spanning 10°–25°N and 110°–120°E at 925 hPa (wind data at 950 hPa are used instead in the 20thCR data set as the latter does not include data at the 925 hPa level). This index corresponds to proxy records covering southern China (Figures 1c and 1d). Winter SSTs averaged over a region spanning 0°–20°N and 40°–80°E covered by core MD77-194 (Figure 1e) were interpreted as an estimates of winter WIO SSTs. Following the removal of long-term trends in both data sets, comparisons (Figure 5) show a significantly negative relationship between the EAWM_S index (based on 20thCR) and WIO SSTs (based on the COBE-SST2 data set) with a correlation coefficient of -0.50 ($P < 0.05$) for the period spanning 1872–1941 and -0.59 ($P < 0.05$) for the period spanning 1956–2012. Further investigation showed that the EAWM indicated by the EAWM_S index does not correlate with the SH (Figure 6, color). The EAWM_S does,

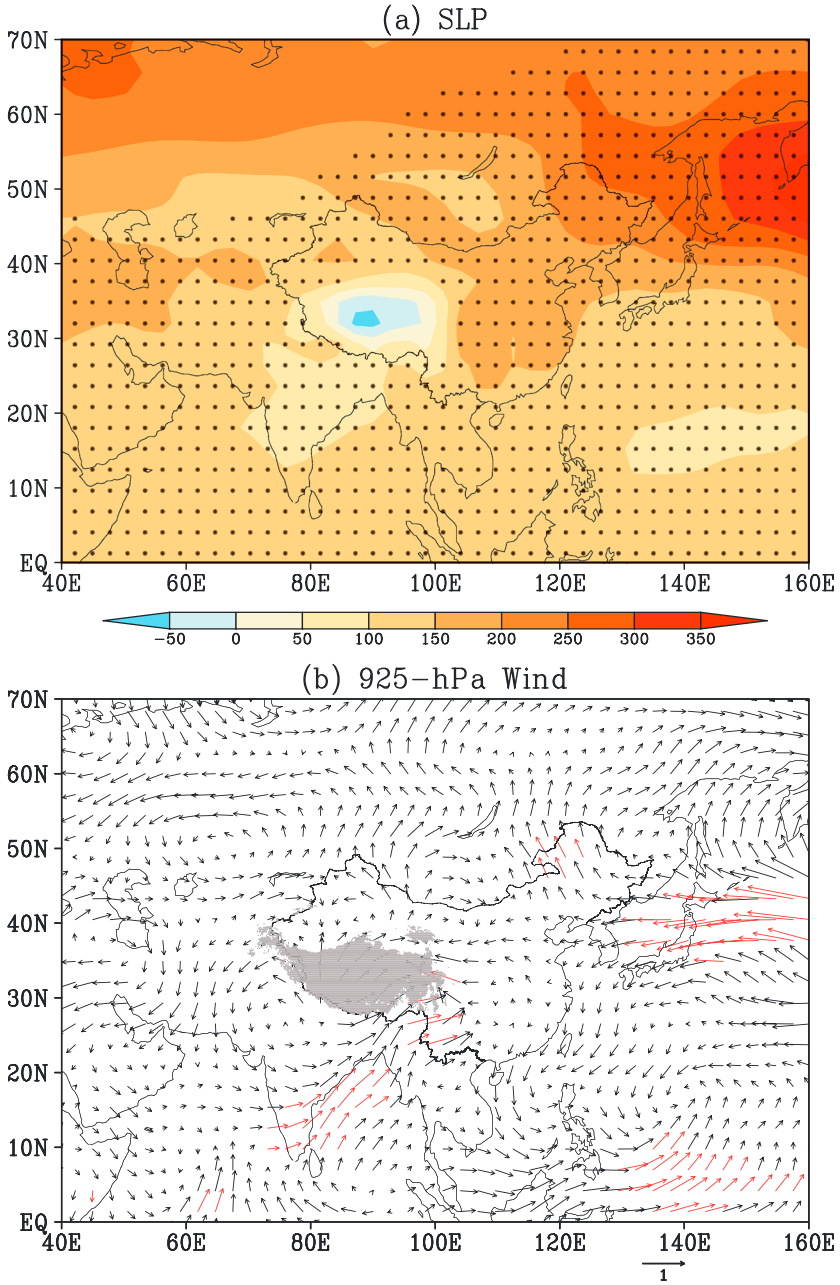

Figure 4. Early Holocene (8.5 ka BP) differences in (a) winter sea level pressure (SLP; Pa) and (b) 925 hPa wind fields (vectors in m/s) as estimated from the CCSM3 8.5 ka equilibrium simulations (Exp_8.5 ka $_{\text{MELTICE}}$ minus Exp_8.5 ka, see Table 3). Stippling and red vectors indicate that differences are significant at the 5% significance level.

however, correlate with a SLP pattern showing positive anomalies over southern China, northern Vietnam, Laos, and Thailand, and negative anomalies over the Philippines and western Pacific (Figure 6, color). These anomalies would give rise to a SLP gradient between Eurasia's southeastern coast and the western Pacific (Figure 6, color), possibly generating northeasterly surface winds (Figure 6, gray vector) that could in turn become a strong EAWM. WIO SSTs are negatively correlated with SLPs over southern China, northern Vietnam, Laos, and Thailand (Figure 6, contours), and therefore have a negative relationship with both the EAWM_S related SLP pattern and the EAWM. The WIO can significantly warm the overlying troposphere, inducing eastward propagating Kelvin waves. These generate significant warming of the western Pacific warm pool (Figure 7) [*Chiang and Sobel*, 2002] causing low-level convergence over southern China, northern

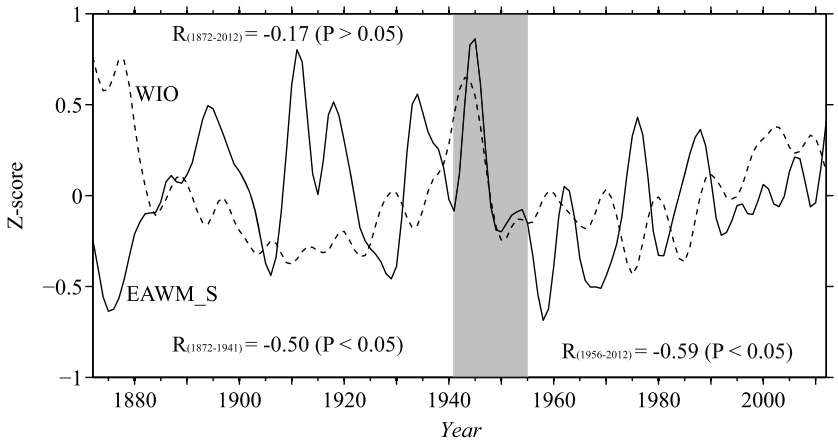

Figure 5. Relationship between the EAWM (time series of the EAWM_S index, solid line) and WIO SSTs (dashed line) from 1872 to 2012. Both time series are normalized and detrended with a nine-point filter.

Vietnam, Laos, and Thailand (Figure 6, contours). Previous studies have suggested that cold, dry air from Siberia associated with a strong EAWM (surface northerlies) could cool the WIO [*Yan et al.*, 2011; *Wang and Wu*, 2012]. Positive feedback between the EAWM (EAWM_S index) and WIO SSTs is, therefore, a potential driving factor for EAWM variability in southern China. During the early Holocene, the SLP gradient over southeastern Asia and associated northerly winds did not show obvious responses to changes in NH ice volume or AMOC strength (Figure 4), which has also been revealed by *Li and Morrill* [2014]. Accordingly, shifts at high latitudes did not influence the EAWM over southern China as strongly as they influenced EAWM expression in northwestern China from 10 to 7.5 ka B.P.

WIO SSTs are furthermore positively correlated with tropospheric temperatures over the Tibetan Plateau (Figure 7), leading to anomalous low pressures (Figure 6, contours) that generate southerly wind anomalies on the eastern Tibetan Plateau. The anomalous southerly winds block dust transport from northwestern China to areas south. Changes in the EAWM occurring in the Huangyanghe area (Figure 2b1) probably relate to the effects of shifting SLPs on the Tibetan Plateau, evident from a decrease in mean grains size from Huangyanghe sediments after about 6 ka B.P. [*Li and Morrill*, 2014]. As during the early Holocene, the

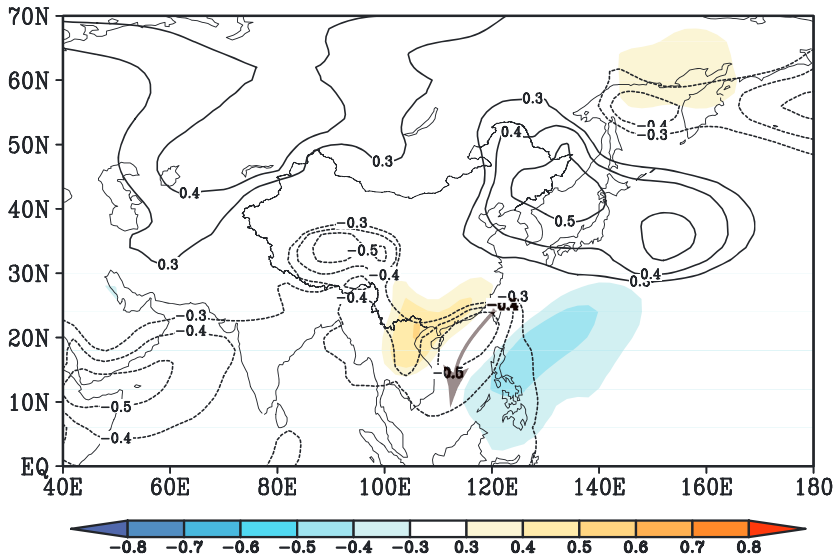

Figure 6. Map showing correlation between winter SLPs (detrended) and EAWM_S index (color) along with WIO SSTs (contours) from 1872 to 2012. Correlation coefficients ≥ 0.3 are significant at the 5% significance level as estimated using Monte Carlo methods [*Livezey and Chen*, 1983; *Di Lorenzo et al.*, 2010].

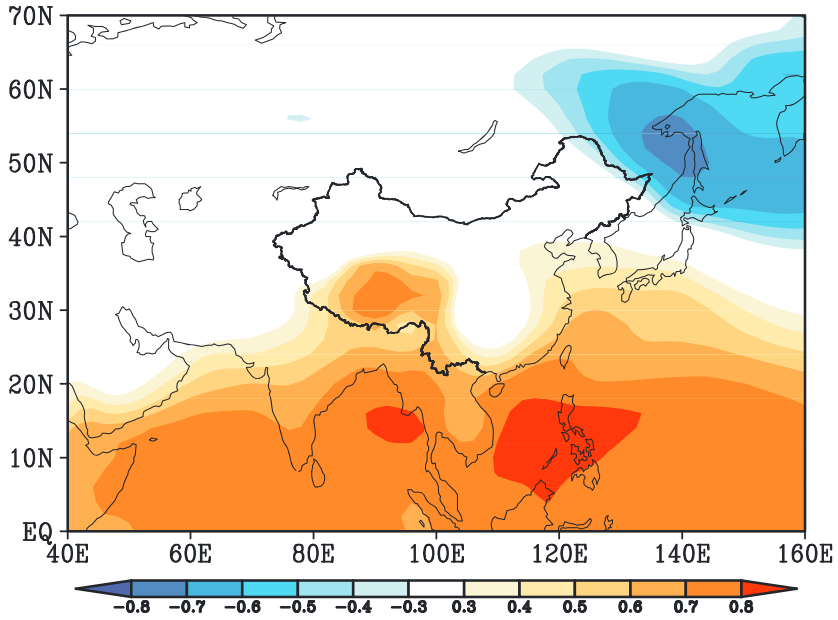

Figure 7. Map showing correlation between winter tropospheric temperatures (1000–500 hPa, detrended) and WIO SSTs (detrended) from 1872 to 2012 on interdecadal time scales. Correlation coefficients ≥ 0.3 are significant at the 5% significance level as estimated using Monte Carlo methods [*Livezey and Chen*, 1983; *Di Lorenzo et al.*, 2010].

effects of SLP variation on the Tibetan Plateau are not statistically significant (Exp_8.5 ka $_{\text{MELTICE}}$ minus Exp_8.5 ka in the CCSM3 8.5 ka B.P. equilibrium simulation, Figure 4a). Changes in NH ice volume and AMOC strength thus may not have influenced EAWM intensity on the eastern Tibetan Plateau.

We analyzed the HT simulation results to further investigate the influence of WIO SSTs on the EAWM. The simulated Holocene EAWM in southern China (EAWM_S index) generates a stronger winter monsoon during the early Holocene than during the late Holocene (Figure 8), which has a close relationship with WIO SSTs (Figure 9) revealed by proxy data (Figure 2c). The timing presented by the simulation was consistent with that observed from proxy estimates of WIO SSTs (Figures 8 and 2c). Similar to their behavior on decadal time scales (Figure 6, color), the EAWM_S index correlates with the SLP gradient over Southeast Asia on millennial time scales (Figure 10, color). The WIO SSTs are also negatively correlated with the EAWM_S related SLP gradient (Figure 10, contours). Reanalysis of data therefore shows that the

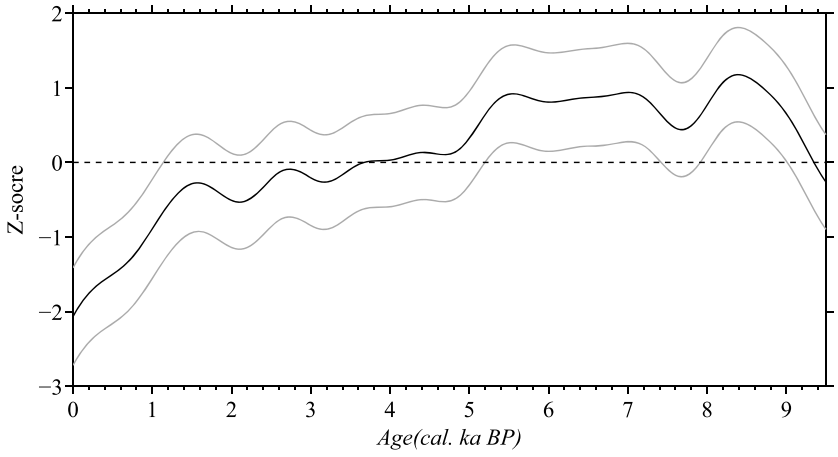

Figure 8. Simulated Holocene East Asian winter monsoon index (EAWM_S index, 99-point filtered) from the HT simulation. The gray envelope shows the 95% confidence interval.

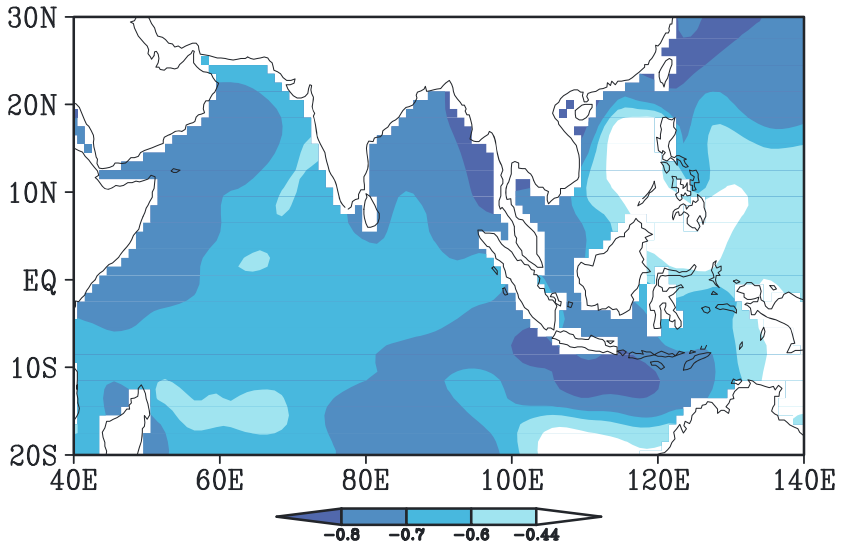

Figure 9. Map showing correlation between simulated winter SSTs (99-point filtered) and EAWM_S index (99-point filtered) from the HT simulation. Correlation coefficients ≥ 0.44 are significant at the 5% significance level as estimated using Monte Carlo methods [*Livezey and Chen*, 1983; *Di Lorenzo et al.*, 2010].

underlying physical mechanisms for EAWM variation from 1872 to 2012 on decadal time scales are quite similar on millennial time scales during the Holocene. Long-term Holocene transient simulation results, however, do not adequately explain the influence of WIO SSTs on EAWM on the eastern Tibetan Plateau, due to complexities in their relationship at this locality (Figure 10, contours). WIO SSTs also have a weaker relationship with SLP data from the Siberian-Mongolian region (Figure 10, contours), indicating that WIO SSTs exert only a weak influence on the winter monsoon over northwestern China.

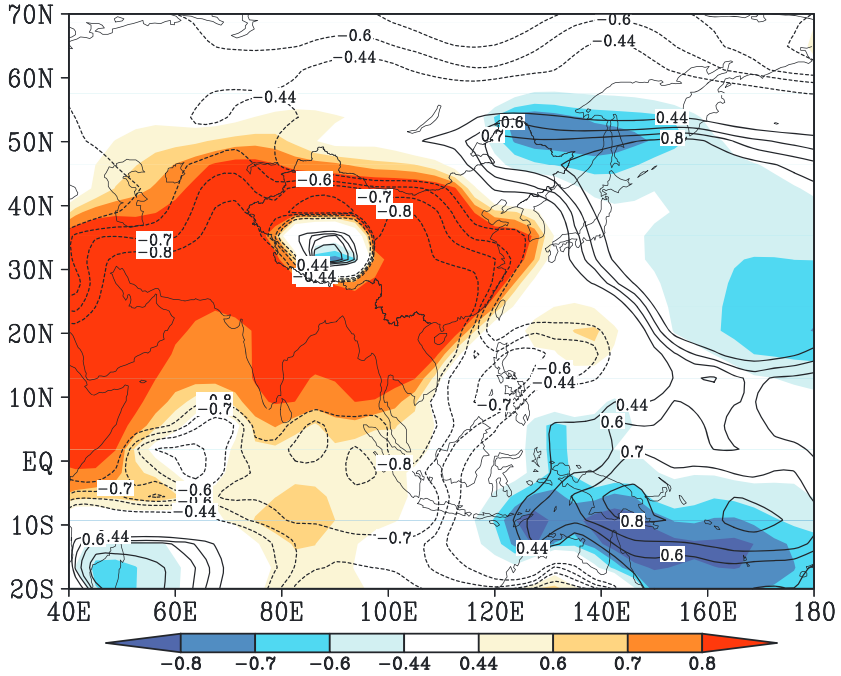

Figure 10. Map showing correlation between simulated winter SLPs and the EAWM_S index (color) along with WIO SSTs (contours) on millennial time scales from the HT simulation. Correlation coefficients ≥ 0.44 are significant at the 5% significance level as estimated using Monte Carlo methods [*Livezey and Chen*, 1983; *Di Lorenzo et al.*, 2010].

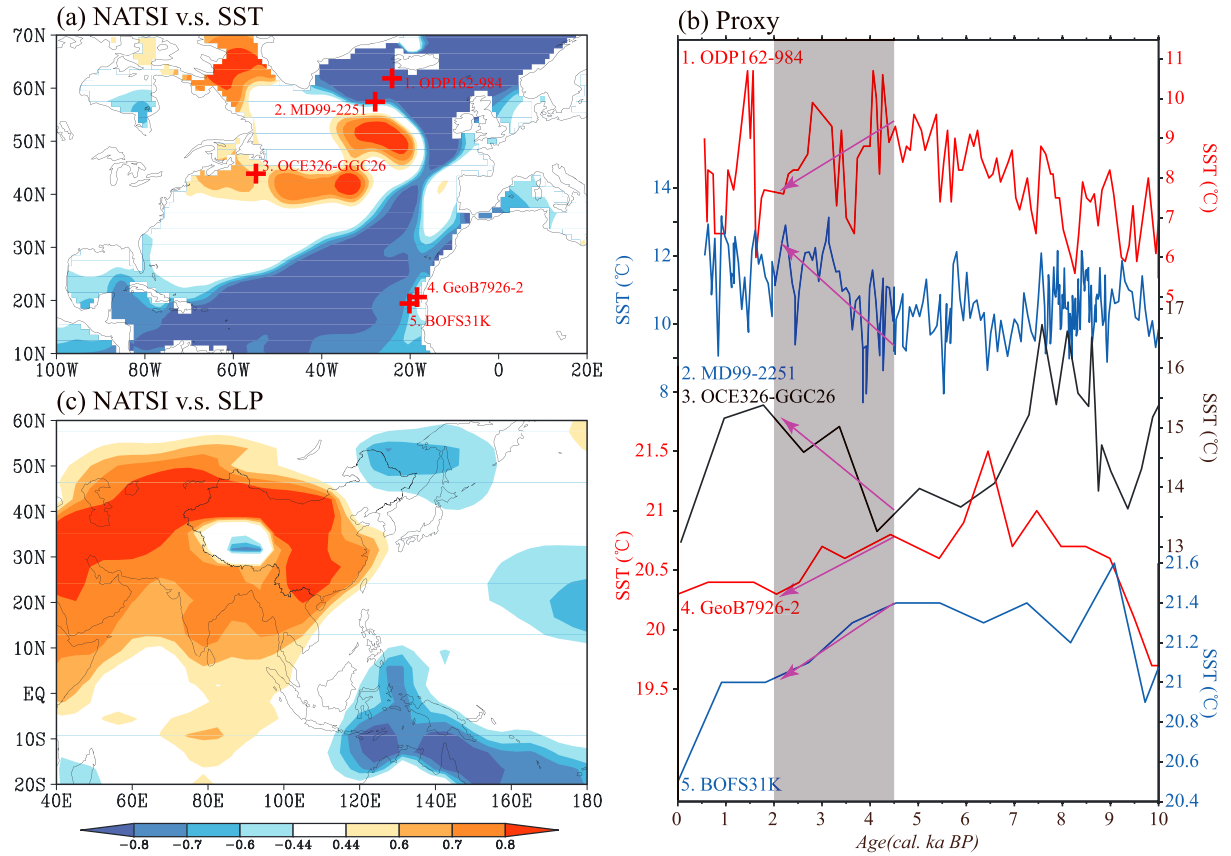

Figure 11. (a) Simulated Holocene North Atlantic winter SST patterns derived from the first empirical orthogonal function (EOF) mode of Holocene DJF SST over North Atlantic (99-point filtered) from the HT simulation, which accounts for 68.86% of the total variance. Crosses indicate the locations of SST proxy records in the North Atlantic. Proxy records includes Mg/Ca data from cores OCE326-GGC26 (43.483°N, 54.867°W) [*Sachs*, 2007], MD99-2251 [*Farmer et al*., 2011], and ODP162-984 [*Came et al*., 2007], and alkenone data from cores MD77-194 (10.4667°N, 75.2333°E) [*Sonzogni et al*., 1998], BOFS31K (19°N, 20.167°W) [*Zhao et al*., 1995], and GeoB7926-2 (20.217°N, 18.45°W) [*Romero et al*., 2008]. (b) Evolution of North Atlantic SSTs observed from proxy data in Figure 11a. (c) Correlation map of winter SSTs (99-point filtered) relative to the principal EOF1 component (PC1, 99-point filtered) during the Holocene. Colored areas indicate correlations that are significant at the 5% significance level as estimated using Monte Carlo methods [*Livezey and Chen*, 1983; *Di Lorenzo et al*., 2010].

Since 4.5 ka B.P., the winter monsoon over northwestern China has become gradually stronger in tandem with a stable but relatively low NH ice volume (Figure 2a2) and enhanced AMOC (Figure 2a3). In areas over the eastern Tibetan Plateau and southern China, the winter monsoon shows a trend (Figure 2b1) similar to that observed around northwestern China, wherein WIO SSTs level off from 4.5 to 2 ka B.P. (Figure 2b2). Consistent variation in winter monsoon intensity in northwestern China, the eastern Tibetan Plateau and southern China from 4.5 to 2.0 ka B.P. probably relate to North Atlantic tripole SSTs (NATS) variability (Figure 11), as described below.

We performed empirical orthogonal function (EOF) analysis on the Holocene North Atlantic winter SSTs, as simulated by the KCM model, to identify major spatial patterns. The leading EOF mode for North Atlantic winter SSTs (component accounting for 68.86% of the total variance) shows a tripole SST pattern in the North Atlantic, which also appears in SST proxy data from 4.5 to 2 ka B.P. (Figure 11b, shaded area). The area of elevated SSTs (MD99-2251 and OCE326-GGC26, Figure 11a) corresponds well with positive anomalies evident in the KCM simulated SST EOF1 (Figure 11a). Decreased SSTs (ODP162-984, GeoB7926-2, and BOFS31K, Figure 11a) also coincide with negative anomalies in the KCM simulated SST EOF1. SSTs derived from core MD99-2251 show an increasing trend from 4.5 to 2 ka B.P. (Figure 11b). The core however was collected from an area at the boundary of negative anomalies identified in the KCM simulated SST EOF1 component (Figure 11a). The NATS correlates positively with the SH and SLP gradient over Southeast Asia (Figure 11c). This provides a possible explanation for enhanced EAWM over northwestern and southern

China from 4.5 to 2 ka B.P. (Figure 2) as the NATS had shifted in phase from negative to positive (Figure 11b). Model results also fail to explain the change in the EAWM over the eastern Tibetan Plateau during this period. Further investigations are therefore necessary to confirm the role of the NATS in influencing EAWM intensity.

5. Conclusions

This study used multiple proxy records and coupled climate model simulations to investigate the asynchronous Holocene evolution of the EAWM. Winter monsoon strength in northwestern China declined rapidly during the early Holocene (10–7.5 ka B.P.). Proxy data indicate that monsoonal decline did not occur on the eastern Tibetan Plateau or in southeastern China until the mid-Holocene (6–4.5 ka B.P.). In northwestern China early Holocene (10–7.5 ka B.P.), monsoonal decline coincided with rapid decrease in NH ice volume and enhanced AMOC. The mid-Holocene (6–4.5 ka B.P.) monsoonal decline affecting the eastern Tibetan Plateau and coastal areas of southeastern China was closely related to an abrupt increase in tropical WIO SSTs. A consistent trend of increasing EAWM intensity in northwestern and southeastern China from 4.5 to 2 ka B.P. probably relates to the NATS variability.

During the early Holocene (10–7.5 ka B.P.), NH ice volume and AMOC exert an apparently strong influence on SH intensity and, by extension, on EAWM intensity at higher latitudes (e.g., northwestern China), but not at lower latitudes (e.g., eastern Tibetan Plateau and southern China). Elevated WIO SSTs influence SLP variation over lower latitudes (e.g., eastern Tibetan Plateau and Southeastern Asia) during the mid-Holocene (6–4.5 ka B.P.). The warmer WIO induced a negative SLP anomaly on the Tibetan Plateau and muted the SLP gradient in southeastern Asia. These effects could generate anomalous southerly winds along the eastern Tibetan Plateau and coastal areas of southeastern China, which counteract northerly winter monsoon winds during the boreal winter, thus weakening the EAWM.

Acknowledgments

Proxy records were provided by authors cited in the text and as follows. Paleo-SST data and ICE-5G data sets were collected from PANGAEA and W.R. Peltier's homepage (http://www.atmosp.physics.utoronto.ca/~peltier/data.php). AMOC data were downloaded from NOAA Paleoclimatology databases. Reanalysis data sets (NCEP/NCAR, 20th Century Reanalysis v. 2, COBE-SST2) were provided by the NOAA/OAR/ESRL PSD, Boulder, Colorado, USA (website: http://www.esrl.noaa.gov/psd/). KCM model simulations were performed at the Computer Center of Kiel University, Germany. Wonsun Park and Latif Mojib of GEOMAR-Helmholtz-Zentrum für Ozeanforschung Kiel, and Birgit Schneider of Christian-Albrechts-Universität zu Kiel provided helpful comments and discussions concerning the KCM Holocene climate simulations. We also thank Carrie Morrill and Bette L. Otto-Bliesner for providing the 8.5 ka B.P. simulations by CCSM3. This work is jointly supported by the National Natural Science Foundation of China (NSFC) (grants 41275071 and 41130102), the National Basic Research Program of China (973 Program) (grants 2010CB950202 and 2010CB950204), and the Fundamental Research Funds for the Central Universities (grant lzujbky-2015-218).

References

An, C., J. Zhao, S. Tao, Y. Lv, W. Dong, H. Li, M. Jin, and Z. Wang (2011), Dust variation recorded by lacustrine sediments from central Asia since ~15 cal kyr BP and its implication for atmospheric circulation, *Quat. Res.*, *75*, 566–573, doi:10.1016/j.yqres.2010.12.015.

An, Z. (2000), The history and variability of the East Asian paleomonsoon climate, *Quat. Sci. Rev.*, *19*, 171–187, doi:10.1016/S0277-3791(99)00060-8.

Berger, A., and M. F. Loutre (1991), Insolation values for the climate of the last 10 million years, *Quat. Sci. Rev.*, *10*, 297–317, doi:10.1016/0277-3791(91)90033-Q.

Came, R. E., D. W. Oppo, and J. F. McManus (2007), Amplitude and timing of temperature and salinity variability in the subpolar North Atlantic over the last 10,000 years, *Geology*, *35*, 315–318.

Chen, J., and S. Q. Sun (1999), East Asian winter monsoon anomaly and variation of global circulation. Part I: A comparison study on strong and weak winter monsoon [in Chinese], *Chin J. Atmos. Sci.*, *23*, 101–111.

Chen, W., H. F. Graf, and R.-H. Huang (2000), The interannual variability of East Asian winter monsoon and its relation to the summer monsoon, *Adv. Atmos. Sci.*, *17*, 48–60.

Chen, W., X.-Q. Lan, L. Wang, and Y. Ma (2013), The combined effects of the ENSO and the Arctic Oscillation on the winter climate anomalies over East Asia, *Chin. Sci. Bull.*, *58*, 1355–1362, doi:10.1007/s11434-012-5654-5.

Chen, Z., R. Wu, and W. Chen (2014), Distinguishing interannual variations of the northern and southern modes of the East Asian winter monsoon, *J. Clim.*, *27*, 835–851, doi:10.1175/JCLI-D-13-00314.1.

Chiang, J. C. H., and A. H. Sobel (2002), Tropical tropospheric temperature variations caused by ENSO and their influence on the remote tropical climate*, *J. Clim.*, *15*, 2616–2631, doi:10.1175/1520-0442(2002)015<2616:TTTVCB>2.0.CO;2.

Clark, M. P., and M. C. Serreze (2000), Effects of variations in East Asian snow cover on modulating atmospheric circulation over the North Pacific Ocean, *J. Clim.*, *13*, 3700–3710, doi:10.1175/1520-0442(2000)013<3700:EOVIEA>2.0.CO;2.

Compo, G. P., et al. (2011), The Twentieth Century Reanalysis Project, *Q. J. R. Meteorol. Soc.*, *137*, 1–28, doi:10.1002/qj.776.

De Garidel-Thoron, T., L. Beaufort, B. K. Linsley, and S. Dannenmann (2001), Millennial-scale dynamics of the east Asian winter monsoon during the last 200,000 years, *Paleoceanography*, *16*(5), 491–502, doi:10.1029/2000PA000557.

Di Lorenzo, E., K. M. Cobb, J. C. Furtado, N. Schneider, B. T. Anderson, A. Bracco, M. A. Alexander, and D. J. Vimont (2010), Central Pacific El Niño and decadal climate change in the North Pacific, *Nat. Geosci.*, *3*, 762–765, doi:10.1038/ngeo984.

Ding, Y. H. (1990), Buildup, air-mass transformation and propagation of Siberian high and its relations to cold surge in East Asia, *Meteor. Atmos. Phys.*, *44*, 281–292, doi:10.1007/BF01026822.

Ding, Z., Z. Yu, N. W. Rutter, and T. Liu (1994), Towards an orbital time scale for Chinese loess deposits, *Quat. Sci. Rev.*, *13*, 39–70, doi:10.1016/0277-3791(94)90124-4.

Ding, Z., T. Liu, N. W. Rutter, Z. Yu, Z. Guo, and R. Zhu (1995), Ice-volume forcing of East Asian winter monsoon variations in the past 800,000 years, *Quat. Res.*, *44*, 149–159, doi:10.1006/qres.1995.1059.

Farmer, E. J., M. R. Chapman, and J. E. Andrews (2011), Holocene temperature evolution of the subpolar North Atlantic recorded in the Mg/Ca ratios of surface and thermocline dwelling planktonic foraminifers, *Glob. Planet. Change*, *79*, 234–243.

Gong, D.-Y., S.-W. Wang, and J.-H. Zhu (2001), East Asian winter monsoon and Arctic Oscillation, *Geophys. Res. Lett.*, *28*, 2073–2076, doi:10.1029/2000GL012311.

Gong, G., D. Entekhabi, and J. Cohen (2003), Modeled Northern Hemisphere winter climate response to realistic Siberian snow anomalies, *J. Clim.*, *16*, 3917–3931, doi:10.1175/1520-0442(2003)016<3917:MNHWCR>2.0.CO;2.

Han, Y., X. Tan, Z. Chen, R. Xiang, and L. Zhang (2010), Magnetic granulometry of recent sediments from the Huguang Maar and its implication for provenience, *Chin. Sci. Bull.*, *55*, 418–424, doi:10.1007/s11434-009-0585-5.

Hays, J. D., J. Imbrie, and N. J. Shackleton (1976), Variations in the Earth's orbit: Pacemaker of the ice age, *Science*, *194*, 1121–1132, doi:10.1126/science.194.4270.1121.

He, C.-X., Y.-H. Ding, and J.-H. He (2008), Response characteristics of the East Asian winter monsoon to ENSO events [in Chinese], *Chin. J. Atmos. Sci.*, *32*, 335–344, doi:10.3878/j.issn.1006-9895.2008.02.12.

Hirahara, S., M. Ishii, and Y. Fukuda (2014), Centennial-scale sea surface temperature analysis and its uncertainty, *J. Clim.*, *27*, 57–75, doi:10.1175/JCLI-D-12-00837.1.

Hu, Z. Z., L. Bengtsson, and K. Arpe (2000), Impact of global warming on the Asian winter monsoon in a coupled GCM, *J. Geophys. Res.*, *105*, 4607–4624, doi:10.1029/1999JD901031.

Huang, E., J. Tian, and S. Steinke (2011), Millennial-scale dynamics of the winter cold tongue in the southern South China Sea over the past 26 ka and the East Asian winter monsoon, *Quater. Res.*, *75*(1), 196–204, doi:10.1016/j.yqres.2010.08.014.

Imbrie, J., J. D. Hays, D. G. Martinson, A. McIntyre, A. C. Mix, J. J. Morley, N. G. Pisias, W. L. Prell, and N. J. Shackleton (1984), The orbital theory of Pleistocene climate: Support from a revised chronology of the marine delta 18O record, in *Milankovitch and Climate*, edited by A. Berger et al., pp. 269–305, Part I. Reidel, Dordrecht, Netherlands.

Ji, L. R., S. Q. Sun, K. Arpe, and L. Bengtsson (1997), Model study on the interannual variability of Asian winter monsoon and its influence, *Adv. Atmos. Sci.*, *14*, 1–22, doi:10.1007/s00376-997-0039-4.

Jin, L., B. Schneider, W. Park, M. Latif, V. Khon, and X. Zhang (2014), The spatial-temporal patterns of Asian summer monsoon precipitation in response to Holocene insolation change: A model-data synthesis, *Quat. Sci. Rev.*, *85*, 47–62, doi:10.1016/j.quascirev.2013.11.004.

Jin, L., F. Chen, C. Morrill, B. L. Otto-Bliesner, and N. Rosenbloom (2012), Causes of early Holocene desertification in arid central Asia, *Clim. Dyn.*, *38*, 1577–1591, doi:10.1007/s00382-011-1086-1.

Jhun, J.-G., and E.-J. Lee (2004), A new East Asian winter monsoon index and associated characteristics of winter monsoon, *J. Clim.*, *17*, 711–726, doi:10.1175/1520-0442(2004)017<0711:ANEAWM>2.0.CO;2.

Kalnay, E., et al. (1996), The NCEP/NCAR 40-year reanalysis project, *Bull. Amer. Meteor. Soc.*, *77*, 437–470, doi:10.1175/1520-0477(1996)077<0437:TNYRP>2.0.CO;2.

Leduc, G., R. Schneider, J.-H. Kim, and G. Lohmann (2010), Holocene and Eemian Sea surface temperature trends as revealed by alkenone and Mg/Ca paleothermometry, *Quat. Sci. Rev.*, *29*, 989–1004.

Li, Y., and C. Morrill (2014), A Holocene East Asian winter monsoon record at the southern edge of the Gobi Desert and its comparison with a transient simulation, *Clim. Dyn.*, doi:10.1007/s00382-014-2372-5.

Lisiecki, L. E., and M. E. Raymo (2005), A Pliocene-Pleistocene stack of 57 globally distributed benthic δ18O records, *Paleoceanography*, *20*, PA1003, doi:10.1029/2004PA001071.

Liu, Q., X. Jiang, S.-P. Xie, and W. T. Liu (2004), A gap in the Indo-Pacific warm pool over the South China Sea in boreal winter, *J. Geophys. Res.*, *109*, C07012, doi:10.1029/2003JC002179.

Liu, T. S., and Z. L. Ding (1998), Chinese loess and the paleomonsoon, *Annu. Rev. Earth Planet. Sci.*, *26*, 111–145, doi:10.1146/annurev.earth.26.1.111.

Livezey, R. E., and W. Y. Chen (1983), Statistical field significance and its determination by Monte Carlo techniques, *Mon. Wea. Rev.*, *111*, 46–59, doi:10.1175/1520-0493(1983)111<0046:SFSAID>2.0.CO;2.

Lorenz, S., and G. Lohmann (2004), Acceleration technique for Milankovitch type forcing in a coupled atmosphere-ocean circulation model: Method and application for the Holocene, *Clim. Dyn.*, *23*, 727–743, doi:10.1007/s00382-004-0469-y.

Lu, E., and J. C. L. Chan (1999), A unified monsoon index for South China, *J. Clim.*, *12*, 2375–2385, doi:10.1175/1520-0442(1999)012<2375:AUMIFS>2.0.CO;2.

McManus, J. F., R. Francois, J. M. Gherardi, L. D. Keigwin, and S. Brown-Leger (2004), Collapse and rapid resumption of Atlantic meridional circulation linked to deglacial climate changes, *Nature*, *428*(6985), 834–837, doi:10.1038/nature02494.

Park, W., N. Keenlyside, M. Latif, A. Ströh, R. Redler, E. Roeckner, and G. Madec (2009), Tropical Pacific climate and its response to global warming in the Kiel Climate Model, *J. Clim.*, *22*, 71–92, doi:10.1175/2008JCLI2261.1.

Peltier, W. R. (2004), Global glacial isostasy and the surface of the ice-age Earth: The ICE-5G (VM2) model and GRACE, *Annu. Rev. Earth Planet. Sci.*, *32*, 111–149, doi:10.1146/annurev.earth.32.082503.144359.

Porter, S. C. (2001), Chinese loess record of monsoon climate during the last glacial-interglacial cycle, *Earth Sci. Rev.*, *54*, 115–128, doi:10.1016/S0012-8252(01)00043-5.

Porter, S. C., and Z. An (1995), Correlation between climate events in the North Atlantic and China during the last glaciation, *Nature*, *375*, 305–308, doi:10.1038/375305a0.

Romero, O. E., J.-H. Kim, and B. Donner (2008), Submillennial-to-millennial variability of diatom production off Mauritania NW Africa, during the last glacial cycle, *Paleoceanography*, *23*, PA3218, doi:10.1029/2008PA001601.

Ruddiman, W. F., M. E. Raymo, D. G. Martinson, B. M. Clement, and J. Backman (1989), Pleistocene evolution: Northern Hemisphere ice sheets and the North Atlantic Ocean, *Paleoceanography*, *4*, 353–412, doi:10.1029/PA004i004p00353.

Sachs, J. P. (2007), Cooling of Northwest Atlantic slope waters during the Holocene, *Geophys. Res. Lett.*, *34*, L03609, doi:10.1029/2006GL028495.

Shackleton, N. J., A. Berger, and W. R. Peltier (1990), An alternative astronomical calibration of the lower Pleistocene time scale based on ODP site 677, *Phil. Trans.*, *81*, 251–261, doi:10.1017/S0263593300020782.

Shi, Z., X. Liu, Y. Sun, Z. An, Z. Liu, and J. Kutzbach (2011), Distinct responses of East Asian summer and winter monsoons to astronomical forcing, *Clim. Past*, *7*, 1363–1370, doi:10.5194/cp-7-1363-2011.

Sonzogni, C., E. Bard, and F. Rostek (1998), Tropical sea surface temperatures during the last glacial period: A view based on alkenones in Indian Ocean sediments, *Quat. Sci. Rev.*, *17*, 1185–1201, doi:10.1016/S0277-3791(97)00099-1.

Steinke, S., M. Mohtadi, J. Groeneveld, L.-C. Lin, L. Löwemark, M.-T. Chen, and R. RendleBühring (2010), Reconstructing the southern South China Sea upper water column structure since the Last Glacial Maximum: Implications for the East Asian winter monsoon development, *Paleoceanography*, *25*, PA2219, doi:10.1029/2009PA001850.

Steinke, S., C. Glatz, M. Mohtadi, J. Groeneveld, Q. Li, and Z. Jian (2011), Past dynamics of the East Asian monsoon: No inverse behaviour between the summer and winter monsoon during the Holocene, *Glob. Planet. Change*, *78*, 170–177, doi:10.1016/j.gloplacha.2011.06.006.

Sun, J., H. Wang, W. Yuan, and H. Chen (2010), Spatial-temporal features of intense snowfall events in China and their possible change, *J. Geophys. Res.*, *115*, D16110, doi:10.1029/2009JD013541.

Sun, Y., X. Wang, Q. Liu, and S. C. Clemens (2010a), Impacts of post-depositional processes on rapid monsoon signals recorded by the last glacial loess deposits of northern China, *Earth Planet. Sci. Lett.*, *289*(1–2), 171–179, doi:10.1016/j.epsl.2009.10.038.

Sun, Y., Z. An, S. C. Clemens, J. Bloemendal, and J. Vandenberghe (2010b), Seven million years of wind and precipitation variability on the Chinese Loess Plateau, *Earth Planet. Sci. Lett.*, *297*, 525–535, doi:10.1016/j.epsl.2010.07.004.
Sun, Y., S. C. Clemens, C. Morrill, X. Lin, X. Wang, and Z. An (2012), Influence of Atlantic meridional overturning circulation on the East Asian winter monsoon, *Nat. Geosci.*, *5*, 46–49, doi:10.1038/ngeo1326.
Tian, J., P. Wang, R. Chen, and X. Cheng (2005), Quaternary upper ocean thermal gradient variations in the South China Sea: Implications for east Asian monsoon climate, *Paleoceanography*, *20*, PA4007, doi:10.1029/2004PA001115.
Tomita, T., and T. Yasunari (1996), Role of the northeast winter monsoon on the biennial oscillation of the ENSO/monsoon system, *J. Meteor. Soc. Jpn.*, *74*, 399–413.
Wang, B. (2006), *The Asian Monsoon*, pp. 779, Springer, Praxis.
Wang, B., R. Wu, and X. Fu (2000), Pacific–East Asian teleconnection: How does ENSO affect East Asian climate?, *J. Clim.*, *13*, 1517–1536, doi:10.1175/1520-0442(2000)013<1517:PEATHD>2.0.CO;2.
Wang, B., Z. Wu, C. P. Chang, J. Liu, J. Li, and T. Zhou (2010), Another look at interannual-to-interdecadal variations of the East Asian winter monsoon: The northern and southern temperature modes, *J. Clim.*, *23*, 1495–1512, doi:10.1175/2009JCLI3243.1.
Wang, H., E. Yu, and S. Yang (2011), An exceptionally heavy snowfall in Northeast china: Large-scale circulation anomalies and hindcast of the NCAR WRF model, *Meteorol. Atmos. Phys.*, *113*, 11–25, doi:10.1007/s00703-011-0147-7.
Wang, L., and R. Wu (2012), In-phase transition from the winter monsoon to the summer monsoon over East Asia: Role of the Indian Ocean, *J. Geophys. Res.*, *117*, D11112, doi:10.1029/2012JD017509.
Wang, L., M. Sarnthein, H. Erlenkeuser, J. Grimalt, P. Grootes, S. Heilig, E. Ivanova, M. Kienast, C. Pelejero, and U. Pflaumann (1999), East Asian monsoon climate during the Late Pleistocene: High-resolution sediment records from the South China Sea, *Mar. Geol.*, *156*, 245–284, doi:10.1016/S0025-3227(98)00182-0.
Wang, L., et al. (2008), Diatom-based inference of variations in the strength of Asian winter monsoon winds between 17,500 and 6000 calendar years B.P, *J. Geophys. Res.*, *113*, D21101, doi:10.1029/2008JD010145.
Wang, L., et al. (2012), The East Asian winter monsoon over the last 15,000 years: Its links to high-latitudes and tropical climate systems and complex correlation to the summer monsoon, *Quat. Sci. Rev.*, *32*, 131–142, doi:10.1016/j.quascirev.2011.11.003.
Watanabe, M., and T. Nitta (1999), Decadal change in the atmospheric circulation and associated surface climate variations in the Northern Hemispheric winter, *J. Clim.*, *12*, 494–510, doi:10.1175/1520-0442(1999)012<0494:DCITAC>2.0.CO;2.
Webster, P. J. (1987), The elementary monsoon, in *Monsoons*, edited by J. S. Fein and P. L. Stephens, pp. 3–32, John Wiley, Hoboken, N. J.
Wu, B.-Y., and R.-H. Huang (1999), Effects of the extremes in the North Atlantic Oscillation on the East Asia winter monsoon, *Chinese J. Atmos. Sci.*, *23*, 226–236.
Wu, B.-Y., and J. Wang (2002), Winter Arctic Oscillation, Siberian high and East Asian winter monsoon, *Geophys. Res. Lett.*, *29*(19), 3-1–3-4, doi:10.1029/2002GL015373.
Wu, B.-Y., R.-H. Zhang, and R. Arrigo (2006), Distinct modes of the East Asian winter monsoon, *Mon. Wea. Rev.*, *134*, 2165–2179, doi:10.1175/MWR3150.1.
Xiao, J. L., T. Nakamura, H. Lu, and G. Zhang (2002), Holocene climate changes over the desert/loess transition of north-central China, *Earth Planet. Sci. Lett.*, *197*, 11–18.
Yan, H., H. Yang, Y. Yuan, and C. Li (2011), Relationship between East Asian winter monsoon and summer monsoon, *Adv. Atmos. Sci.*, *28*, 1345–1356, doi:10.1007/s00376-011-0014-y.
Yancheva, G., N. R. Nowaczyk, J. Mingram, P. Dulski, G. Schettler, J. F. W. Negendank, J. Liu, D. M. Sigman, L. C. Peterson, and G. H. Haug (2007), Influence of the Intertropical Convergence Zone on the East Asian monsoon, *Nature*, *445*, 74–77, doi:10.1038/nature05431.
Yang, S., K. M. Lau, and K. M. Kim (2002), Variations of the East Asian jet stream and Asian-Pacific-American winter climate anomalies, *J. Clim.*, *15*, 306–325, doi:10.1175/1520-0442(2002)015<0306:VOTEAJ>2.0.CO;2.
Yeager, S., C. Shields, W. Large, and J. Hack (2006), The low-resolution CCSM3, *J. Clim.*, *19*, 2545–2566.
Young, J. A. (1987), Physics of monsoon: The current view, in *Monsoons*, edited by J. S. Fein and P. L. Stephens, pp. 211–243, John Wiley, Hoboken, N. J.
Yu, X., W. Zhou, Z. Liu, and Z. Kang (2011), Different patterns of changes in the Asian summer and winter monsoons on the eastern Tibetan Plateau during the Holocene, *The Holocene*, *21*, 1031–1036, doi:10.1177/0959683611400460.
Zhang, R., A. Sumi, and M. Kimoto (1996), Impact of El Niño on the East Asian monsoon: A diagnostic study of the '86/87 and '91/92 events, *J. Meteor. Soc. Jpn.*, *74*, 49–62.
Zhang, Y., K. R. Sperber, and J. S. Boyle (1997), Climatology and interannual variation of the East Asia winter monsoon: Results from the 1979–95 NCEP/NCAR reanalysis, *Mon. Wea. Rev.*, *125*, 2605–2619, doi:10.1175/1520-0493(1997)125<2605:CAIVOT>2.0.CO;2.
Zhang, Z. Y., W. L. Guo, D. Y. Gong, and S.-J. Kim (2013), Evaluation of the twentieth century reanalysis dataset in describing East Asian winter monsoon variability, *Adv. Atmos. Sci.*, *30*(6), 1645–1652, doi:10.1007/s00376-012-2226-1.
Zhao, M., N. A. S. Beveridge, N. J. Shackleton, M. Sarnthein, and G. Eglinton (1995), Molecular stratigraphy of cores off northwest Africa: Sea surface temperature history over the last 80 ka, *Paleoceanography*, *10*, 661–675, doi:10.1029/94PA03354.
Zhou, H., H. Guan, and B. Chi (2007), Record of winter monsoon strength, *Nature*, *450*, E10–E11, doi:10.1038/nature06408.
Zhou, H., B. Wang, H. Guan, Y. Lai, C. You, J. Wang, and H. Yang (2009), Constraints from strontium and neodymium isotopic ratios and trace elements on the sources of the sediments in Lake Huguang Maar, *Quat. Res.*, *72*(2), 289–300, doi:10.1016/j.yqres.2009.06.005.